Heliyon 10 (2024) e33193

Contents lists available at ScienceDirect

Heliyon

journal homepage: www.cell.com/heliyon

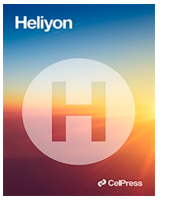

Research article

Bioinformatic analysis indicated that STARD4-AS1 might be a novel ferroptosis-related biomarker of oral squamous cell carcinoma

Jiahui Li [1], Zihe Qiao [1], Yuwei Li, Xinyan Lu, Tingru Shao [**], Xiaozhi Lv [*]

Department of Oral and Maxillofacial Surgery, Zhujiang Hospital, Southern Medical University, Guangzhou, 510280, China

ARTICLE INFO

Keywords:
Oral squamous cell carcinoma
Ferroptosis
Long non-coding RNAs
Bioinformatics
Prognosis
STARD4-AS1

ABSTRACT

Background: Oral squamous cell carcinoma (OSCC) stands as the predominant form of oral cancer, marked by a poor prognosis. Ferroptosis, a type of programmed cell death, plays a critical role in the initiation and progression of various cancers. Long non-coding RNAs (lncRNAs) are prominent in modulating cancer development. Nevertheless, the prognostic significance of ferroptosis-related lncRNAs (FRLs) in OSCC remains inadequately explored. This study aims to develop a predictive signature based on FRLs to forecast the prognosis of OSCC patients.

Methods: We gathered expression profiles of FRLs along with clinical data from The Cancer Genome Atlas (TCGA) and FerrDb databases. A prognostic model based on 10 FRLs were constructed using Cox regression analyses with LASSO algorithms, and their predictive power was evaluated. Then, the model was used to investigate functional enrichment, immune landscape, m6A genes, somatic variations, and drug response in different risk cohorts of patients. Finally, the expression and function of STARD4-AS1 (steroidogenic acute regulator protein-related lipid transfer domain containing 4-antisense RNA 1), a potential prognostic marker for OSCC screening based on our bioinformatics analysis, were investigated in vitro.

Results: We developed a signature comprising 10 FRLs to stratify patients into two risk cohorts according to their calculated risk scores. Patients classified as high-risk exhibited significantly poorer prognoses compared to those in the low-risk cohort. Furthermore, survival analysis, patient risk heat plot, and risk curve verified the accuracy of the signature. The role of this signature in OSCC was well investigated using immune microenvironment, mutational, and gene set enrichment analysis (GSEA). Moreover, seven drugs, including cisplatin and docetaxel, were identified as potential treatments for patients with high-risk cancers. In addition, the knockdown of STARD4-AS1 in OSCC cell lines markedly inhibited cell proliferation and migration and induced ferroptosis.

Conclusion: Using this signature may improve overall survival predictions in OSCC, throwing new light on immunotherapies and targeted therapies. Moreover, STARD4-AS1 might regulate the process of ferroptosis and could be used as a novel biomarker of OSCC.

* Corresponding author.
** Corresponding author.
E-mail addresses: star0212@smu.edu.cn (T. Shao), lvxiaozhi@smu.edu.cn (X. Lv).
[1] The two authors contributed equally to this paper.

https://doi.org/10.1016/j.heliyon.2024.e33193
Received 19 December 2023; Received in revised form 11 June 2024; Accepted 16 June 2024
Available online 17 June 2024

1. Introduction

Oral squamous cell carcinoma is among the most prevalent head and neck cancers, characterized by its aggressive nature and resistance to conventional treatments like chemotherapy and radiotherapy [1]. In 2022, OSCC was responsible for 11,230 deaths globally [2]. Several therapeutic strategies are available for OSCC. Gene-targeted therapy has emerged as a prominent approach for treating various tumors. Notably, targeted therapy for cancer stem cells, implicated as a cause of OSCC metastasis and resistance to chemotherapy or radiotherapy, may be a useful strategy for treating OSCC [3,4]. In addition, tumor immunotherapy has shown clinical efficacy in treating cancers with high mutational load and microsatellite instability, such as OSCC [5–7]. Despite this, only 50 % of patients with OSCC survive five years after diagnosis [2]. Therefore, a new non-invasive prognostic model and effective therapeutic targets are required to facilitate early diagnosis of OSCC and optimize treatment to improve the prognosis in patients.

Iron, a crucial transition metal, is indispensable for the rapid growth and proliferation of cancer cells. Ferroptosis, an iron-dependent form of programmed cell death, is governed by various metabolic pathways and characterized by the accumulation of lipid peroxides [5,8,9]. Notably, cancer cells that exhibit resistance to conventional therapies or possess a high metastatic potential are particularly susceptible to ferroptosis [6,7]. Therefore, ferroptosis induction is being explored as a latent cancer therapy target [10–12]. Multiple chemotherapy-resistant tumors may respond well to ferroptosis inducers [13,14], and induction of ferroptosis may guard against acquired resistance to several cancer therapies [6,7,15]. Ferroptosis plays a prominent role in the pathogenesis of OSCC. Histone deacetylase inhibitors, such as quisinostat, markedly inhibit the activity of tongue squamous cell carcinoma cells by inducing ferroptosis. Additionally, various drugs like eliglustat (CB839) and innovative materials such as zero-valent iron nanoparticles have been proposed to enhance treatment efficacy against head and neck squamous cell carcinoma by leveraging the mechanisms of ferroptosis [16–18]. Hence, it is imperative to explore the potential mechanisms underlying ferroptosis-associated genes in OSCC.

Approximately 70 % of the human transcriptome comprises [19]. LncRNA mutations and dynamic changes in expression are closely related to tumorigenesis, progression, and metastasis. Remarkably, lncRNAs can inhibit or promote programmed cell death by directly or indirectly regulating protein complexes and microRNAs in cancer cells [20,21]. According to Liu et al., certain lncRNAs possess the capability to instigate ferroptosis within malignant cells, thereby manifesting anticancer properties. Breast cancer metastasis is inhibited by lncRNA metastasis-associated lung adenocarcinoma transcript 1 (MALAT1) [21]. LncRNAs are overexpressed in OSCC cells and promote tumor progression by enhancing proliferation and migration [22]. However, there remains a considerable paucity of research exploring the prognostic value of FRLs in OSCC. Consequently, it is imperative that FRL expression and regulation be explored in OSCC cells.

Here, our study centered on the correlation between ferroptosis-related lncRNAs and the prognosis of OSCC patients, and further investigated to unearth the potential mechanisms. Within the research, we constructed a prognostic signature comprising ferroptosis-related lncRNAs, which can enhance the overall survival prediction of OSCC and provide emerging ideas for the selection of immunotherapies, targeted therapies, and chemotherapeutic agents. We also explored a novel biomarker, STARD4-AS1, which offers inspiration for more nuanced inquiries into the realm of ferroptosis within OSCC in the future.

2. Material and methods

2.1. Data collection

The TCGA database (https://tcga-data.nci.nih.gov/tcga/; website access date: February 15, 2022) contained the clinical data and RNA-seq transcriptome information associated with OSCC. OSCC patient samples were drawn from this database, comprising a total of 305 tissue specimens, of which 276 originated from OSCC tissues and 29 were sourced from adjacent normal tissues. We collected the clinicopathologic data, which included gender, age, tumor grade, survival time, and survival status. On October 15, 2021, somatic mutation data based on the TCGA-OSCC dataset were imported from the Genomic Data Commons (GDC) database for the whole-exome sequencing platform. GTF data were downloaded to distinguish mRNAs from lncRNAs through Ensembl (http://asia.ensembl.org; website access date: June 5, 2021). Ferroptosis-related genes (FRGs) that have been identified were compiled from FerrDb (http://www.zhounan.org/ferrdb/; website access date: March 1, 2022)., and FRLs were screened using a co-expression strategy after removing duplicates.

2.2. Identification of ferroptosis-related differentially expressed (DE)-lncRNAs

We retrieved the expression of 14,086 lncRNAs from the TCGA database, and 388 FRGs were drawn from the FerrDb website. The relation between lncRNAs and FRGs was explored through the application of Pearson's correlation analysis. Subsequently, 1504 FRLs were identified using Spearman correlation analysis based on the threshold values of $|cor| \geq 0.4$ and $P < 0.05$. The raw data were manipulated using the "DESeq2" package in R software version 4.0.5. LncRNAs with $|log2FoldChange| \geq 1$ and FDR <0.05 were identified as DE lncRNAs.

2.3. Creating and confirming the prognostic DE-FRLs signature

In a 1:1 ratio, patients ($n = 305$) were divided into the validation and discovery cohorts at random. In addition, we included an entire cohort in our analysis for validating the FRLs signature. We constructed a prognostic FRLs signature for the discovery cohort. LASSO regression analysis with 1000 cycles was conducted after univariate Cox risk regression analysis ($P < 0.05$) to identify lncRNAs

linked to overall survival (OS). The following formula was used to calculate the LASSO risk: Lasso risk $= \sum_{i=1}^{n} Coef_i^* x_i$. Utilizing the median risk score derived from the discovery cohort, patients within both the validation and entire cohorts were categorized into high-risk or low-risk cohorts.

The Kaplan–Meier (KM) survival curve was plotted with the high- and low-risk cohorts using the R package "survminer" for comparing the OS duration and validating the prognostic FRL signature. Receiver operating characteristic curve (ROC) analysis was performed using the R package "timeROC" to assess the prediction accuracy of the FRLs signature. To estimate individualized risk scores in OSCC patients. We then performed an independent prognostic analysis to confirm whether characteristics and risk score are independent prognostic factors in predicting OS of patients with OSCC, and the results were presented as a forest map. In the discovery, validation, and entire cohorts, all validations were carried out concurrently. A nomogram was developed from the complete TCGA dataset through multivariate Cox regression analysis incorporating FRLs and various clinicopathologic covariates. Furthermore, internal validation was conducted to evaluate the nomogram's prognostic accuracy.

2.4. Visualization of the lncRNA–mRNA co-expression

LncRNA-mRNA pairs exhibiting a Pearson correlation coefficient (R^2) surpassing 0.4 with a corresponding significance level (P) below 0.05 were identified as promising regulatory pathways. Subsequently, the ferroptosis-associated lncRNA-mRNA co-expression network was visualized using Cytoscape (ver. 3.8.2).

2.5. Functional enrichment analysis

Employing the "clusterProfifiler" R package, we undertook Gene Ontology (GO) and Kyoto Encyclopedia of Genes and Genomes (KEGG) pathway enrichment analyses. The outcomes of our functional enrichment exploration were portrayed utilizing the "GOplot" and "ggplot2" R packages.

2.6. Gene set enrichment analysis

To delve into the potential functional pathways implicated in the FRLs signature, we conducted gene set enrichment analysis (GSEA). Utilizing Java GSEA 3.0 on the KEGG dataset, specifically c2.cp.kegg.v7.2.symbols.gmt, we deemed results with a false discovery rate <0.05 as statistically significant.

2.7. Immune status and gene expression analyses

We scrutinized the differences in immune cell abundance between high- and low-risk cohorts classified by FRLs signatures using the TIMER, CIBERSORT, CIBERSORT-ABS, QUANTISEQ, MCPCOUNTER, XCELL, and EPIC algorithms. In addition, we determined the differential infiltrating scores of immune cells and immune-linked functions between the two cohorts via single sample gene set enrichment analysis (ssGSEA). The variance in the expression level of immune checkpoint inhibitors and m6A-related genes among the cohorts was thoroughly examined.

2.8. Somatic variant analysis

The examination of Mutation Annotation Format files was conducted utilizing the R package "maftools".

2.9. Significance of FRLs in drug sensitivity

Using the R package "pRRophetic" to calculate the IC50 values of chemotherapeutic agents currently employed in the clinical practice. Thirty popular anticancer medications, including axitinib, doxorubicin, gefitinib, pyrimethamine, and vinblastine, are recommended by the American Joint Committee on Cancer guidelines for combating cancer. Employing the Wilcoxon signed-rank test, we scrutinize the variance in IC50 values among 30 antitumor agents, discerning disparities between cohorts categorized as high-risk and low-risk.

2.10. Cell culture and transfection

The repository of Southern Medical University in Guangzhou, China, provided us with the normal oral epithelial cell line (HOK) alongside a cadre of human OSCC cell lines, namely SCC9, SCC15, SCC25, and CAL27. The culture medium used for HOK, SCC9, SCC15, and SCC25 cells was Dulbecco's modified Eagle's medium F12 (DMEM/F12) (Gibco; Cat#11320033), and CAL27 cells were cultured in α-MEM (Gibco; Cat# C12571500BT-10). The silencing RNA against STARD4-AS1 (si-STARD4-AS1) was purchased from Kidan Biosciences Limited. The sequences of si-STARD4-AS1 are shown in the following Table 1. Lipofectamine 3000 (ThermoFisher; Cat#L3000015) was used to transfect siRNA and its negative control.

2.11. Cell viability and proliferation assays

200 μL of DMEM/F12 culture medium was added to each well of 96-well plates to support the growth of SCC9 and SCC15 cells (2 × 103 cells/well). Each cohort was tested in three replicates. Cell viability was assessed at 0, 24, 48, 72, and 96 h following si-RNA induced knockdown using the cell counting kit-8 (CCK-8; KEYGEN BIOTEC, Cat#KGA317s-1000). Following a 72-h treatment with STARD4-AS1 knockdown, SCC9, and SCC15 cells were sealed in 6-well plates. After 7 days, cells were immobilized in methanol and stained with Giemsa dye. Visible colony numbers were counted under the microscope and the colony-forming capacity was determined (visible colonies/seeded cells × 100 %).

2.12. Wound healing and invasion assays

Employing the wound healing assay, we embarked upon an exploration of cellular migration. Cultivated within the confines of 6-well plates, the SCC9 and SCC15 cells were nurtured to 80 % confluence. A wound was crafted using a 200-μL plastic pipette tip. Subsequently, cell migration was observed and quantified at 0 and 24 h.

The assessment of invasiveness was conducted employing the esteemed 24-well BioCoat cell culture inserts, covered with Matrigel courtesy of BD Biosciences in San Jose, CA, USA. Approximately 5 × 104 transfected cells were plated onto the upper chambers in 100 μL serum-free F12, while 600 μL F12 containing 30 % fetal bovine serum was filled with the lower chambers. Fix the filter membrane with 4 % methanol, then stain with 0.1 % crystal violet after 36 h. Evaluate the cell invasion ability by counting the number of cells migrated to the underside of the filter membrane.

2.13. Quantitative real-time polymerase chain reaction (qRT-PCR)

Using the TRIzol reagent (Vazyme; Cat# R401-01) to extract the total RNA from tissues and cells. qRT-PCR was performed using SYBR Green I (Vazyme, Cat#Q711-02) in triplicates. Different gene expressions were compared to GAPDH's expression. The following are the primer sequences (Table 2).

2.14. Reactive oxygen Species (ROS) Detection

Employing the ROS assay kit (Glpbio; Cat#C11 BODIPY 581/591), the levels of cytosolic ROS were measured. To achieve 80 % confluence, cells were treated in PBS with 10 mM dichloro-dihydro-fluorescein diacetate (DCFH-DA) at 37 °C for 30 min in the dark. The stained cells were collected and washed with PBS. The fluorescence intensity of DCFH-DA was detected at 488 nm using a flow cytometer (BD, Fortessa).

2.15. Determination of Fe^{2+} levels

The abundance of Fe^{2+} was quantified through the iron assay kit (Sciencell; Cat# 8448). Cells transfected for 48 h were nurtured within the chambers of a 96-well plate and treated for 30 min using the kit's reagents to quantify Fe^{2+} levels.

2.16. Transmission electron microscope (TEM)

After being inoculated into 6-well plates, SCC9 and SCC15 cells underwent a 48-h transfection. The cells were embedded after being fixed. The embedding blocks into sections measuring 60 nm in diameter, then delicately imbued with uranyl acetate and lead citrate. The ultrastructure images of mitochondria were observed by using a transmission electron microscope.

2.17. Statistical analysis

Statistical scrutiny was conducted employing GraphPad Prism 9.0 (GraphPad Software, La Jolla, CA) and R software version 4.0.5. $P < 0.05$ was deemed statistically significant.

Table 1
The sequences of si-STARD4-AS1 and normal control.

	Primers	Sequence(5'→3')
homo lncRNA	forward	GCUCUUCACUUCUUACAAAUUTT
STARD4-AS1-si1	reverse	AAUUUGUAAGAAGUGAAGAGCTT
homo lncRNA STARD4-AS1-si2	forward	GCGAAACAGUUCAGAACAAGGTT
	reverse	CCUUGUUCUGAACUGUUUCGCTT
homo lncRNA STARD4-AS1-si3	forward	GGACAAAUGAAGAGUUCAAUGTT
	reverse	CAUUGAACUCUUCAUUUGUCCTT
Normal control	forward	UUCUCCGAACGUGUCACGUTT
	reverse	ACGUGACACGUUCGGAGAATT

Table 2
The sequences of STARD4-AS1 and normal control.

	Primer	Sequence(5'→3')
homo lncRNA STARD4-AS1	forward	CTGTTGTGTAAGCTGCCCAG
	reverse	TCAAATGCCCTCCCAGATGT
Normal control	forward	CCAGGTGGTCTCCTCTGACTTC
GAPDH	reverse	GTGGTCGTTGAGGGCAATG

3. Results

3.1. Identification of FRLs and clinical data of patients with OSCC

Fig. 1 visualizes the schematic delineation of the research design flow. First, 14086 lncRNAs were identified in the TCGA-OSCC dataset and 363 FRGs were extracted from the OSCC patient dataset. A Pearson correlation analysis was conducted to elucidate the relationship between these FRGs and lncRNAs, and 1504 FRLs were obtained. The connection between FRGs (red circles) and FRLs (green circles) was visualized with Cytoscape (Fig. 2). One case was removed from the dataset for the lack of survival information and 305 patients with OSCC were finally included in the study. Patient profiles are summarized in Table 3. The patients were split into two cohorts at random: a testing cohort (n = 152) and a training cohort (n = 153).

3.2. DE-lncRNAs

We identified 442 DE-lncRNAs (83 downregulated and 359 upregulated) by comparing tumor samples with adjacent tissue samples. The volcano plot and heatmap (Fig. 3 A, B) of DE-lncRNAs were created using these data.

3.3. Construction of prognostic FRLs signature

A prognostic signature comprising FRLs was crafted utilizing the training cohort, and the other variables in this cohort were validated by LASSO regression analysis. Based on the LASSO regression, ten FRLs were found (Fig. 3C, D). The following formula was

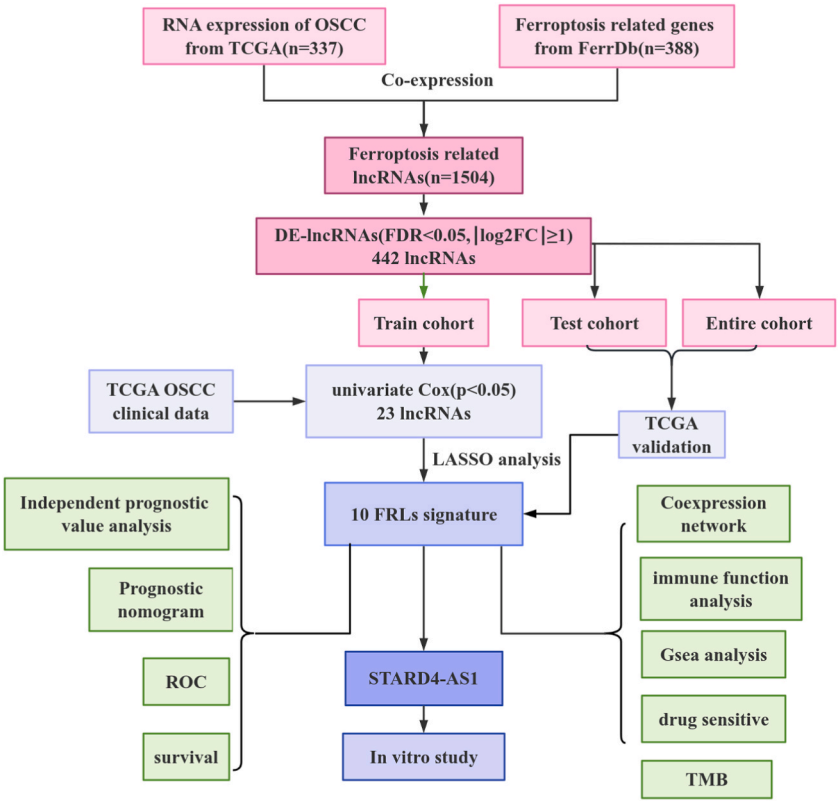

Fig. 1. Flowchart of the study design.

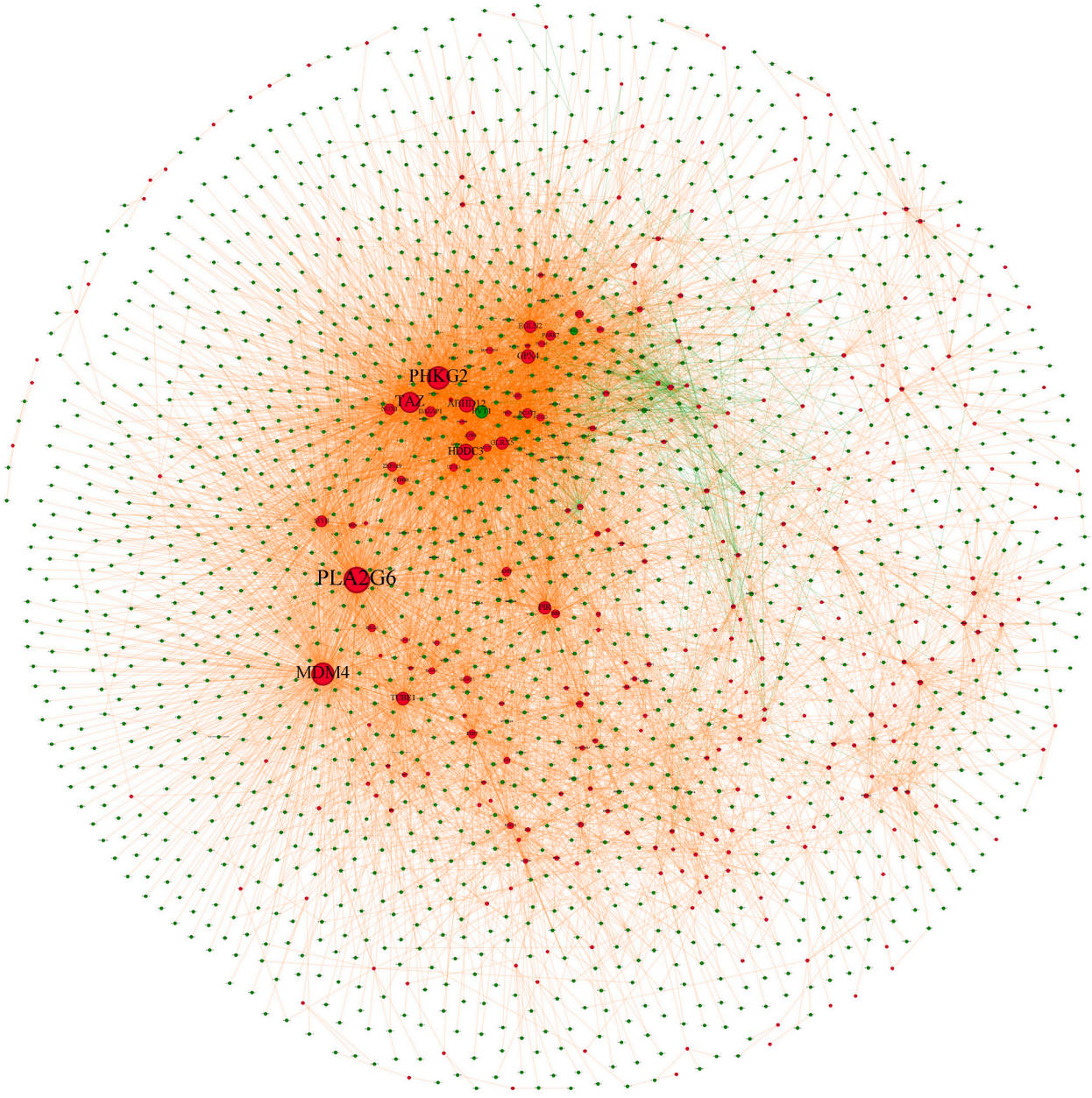

Fig. 2. Co-expression network diagrams of FRGs (red circles) and FRLs (green circles).

used to establish an FRLs signature (Table 4): Risk score = (0.034265893 × expressed value of AC099850.4) + (−0.269102262 × expressed value of AP002807.1) + (1.058285564 × expressed value of AC083967.1) + (0.577269267 × expressed value of AL589986.2) + (0.069335916 × expressed value of AC002401.4) + (−0.710877306 × expressed value of LINC02158) + (−1.666213019 × expressed value of STARD4-AS1) + (0.057968249 × expressed value of LINC02154) + (0.034319589 × expressed value of AL162413.1) + (−0.05733257 × expressed value of AL512274.1). Fig. 3 E shows the forest plot of the relationships of the ten lncRNAs with OS. The connection between FRLs (yellow squares) and FRGs (blue circles) was visualized with Cytoscape (Fig. 3 F). Fig. 3 G shows the network of these FRLs and FRGs as a Sankey diagram.

3.4. Confirming the lncRNA signature

The patients were categorized into high-risk and low-risk cohorts according to a prognostic model derived from 10 FRLs. To validate the classification efficacy of the risk signature, we employed risk curves and scatter plots across the training, testing, and entire cohorts (Fig. 4A–C). Our analysis revealed a higher incidence of mortality in the high-risk cohort compared to the low-risk cohort. The

Table 3
The foundational clinical attributes of the cohort of oral squamous cell carcinoma patients enrolled in this investigation.

	Clinical characteristics	Training cohort (n = 153)	Testing cohort (n = 152)	Entire cohort (n = 305)
Age				
	<65	91	84	175
	≥65	62	68	130
Gender				
	Male	49	50	99
	Female	104	102	206
Grade				
	G1	22	29	51
	G2	103	82	185
	G3	26	38	64
	GX- unknown	2	3	5
Stage				
	Stage I	9	8	17
	Stage II	27	25	52
	Stage III	24	30	54
	Stage IV	80	78	158
	unknown	13	11	24
T				
	T1	15	12	27
	T2	45	49	94
	T3	28	28	56
	T4	56	52	108
	TX- unknow	9	11	20
N				
	N0	64	50	114
	N1	21	24	45
	N2	48	49	97
	N3	1	1	2
	NX-unknown	19	28	47
M				
	M0	57	57	114
	MX-unknown	96	95	191

expressions of 10 FRLs included in the prognostic signature are presented as a heatmap in Fig. 4 D-F. The KM survival analysis demonstrated that the high-risk cohort exhibited a significantly shorter OS compared to the low-risk cohort (Fig. 4 G). By employing the ROC curve analysis, we also evaluated the prognostic accuracy of our model. The AUC predictions for 1-, 3-, and 5-year survival in the training cohort were 0.793, 0.782, and 0.789, respectively (Fig. 4 J). Additionally, we confirmed the prognostic power and accuracy of the 10 FRLs between the test and entire cohorts. In line with the validation cohort results, the OS in the high-risk cohort was considerably lower compared to the low-risk cohort (Fig. 4H, I). The AUC value for the test cohort at one year was 0.641, while for the entire cohort, it was 0.710 (Fig. 4 K, L). To ascertain whether the prognostic model based on FRLs is an independent risk factor for OSCC patients, univariate and multivariate Cox regression analyses were carried out (Fig. 5 A, B). The result revealed that staging and risk score were identified as independent risk variables.

3.5. Correlation of the 10 FRLs with clinical characteristics

The heatmap illustrated the clinicopathologic characteristics of the low- and high-risk cohorts and revealed a statistical disparity in T stages of OSCC between the two cohorts (Fig. 5C). We further stratified each subgroup according to clinicopathologic characteristics. The results were stratified into subgroups according to age, gender, T stage, N stage, clinical stage, and grade (Fig. 5D–O). Across all these categories, the overall survival in the high-risk cohort was markedly lower than in the low-risk cohort.

3.6. Construction and evaluation of the nomogram

By conducting multivariable Cox regression analysis incorporating the prognostic model and additional clinicopathologic covariables, we created a nomogram facilitating clinical prediction of patient survival. Scoring based on different clinicopathologic features and risk cohorts can predict the survival rate of 1-, 3-, and 5-year in OSCC patients (Fig. 5 P). The AUCs of the nomogram for 1-, 3-, and 5-years were 0.719, 0.781, and 0.791, indicating that the nomogram had high specificity and sensitivity for predicting OS (Fig. 5 Q). Furthermore, we performed calibration curve analyses to assess the degree of agreement between the actual survival rate and the survival rate predicted by the nomogram (Fig. 5 R). Our findings indicated that the predicted survival time was quite consistent with the actual results.

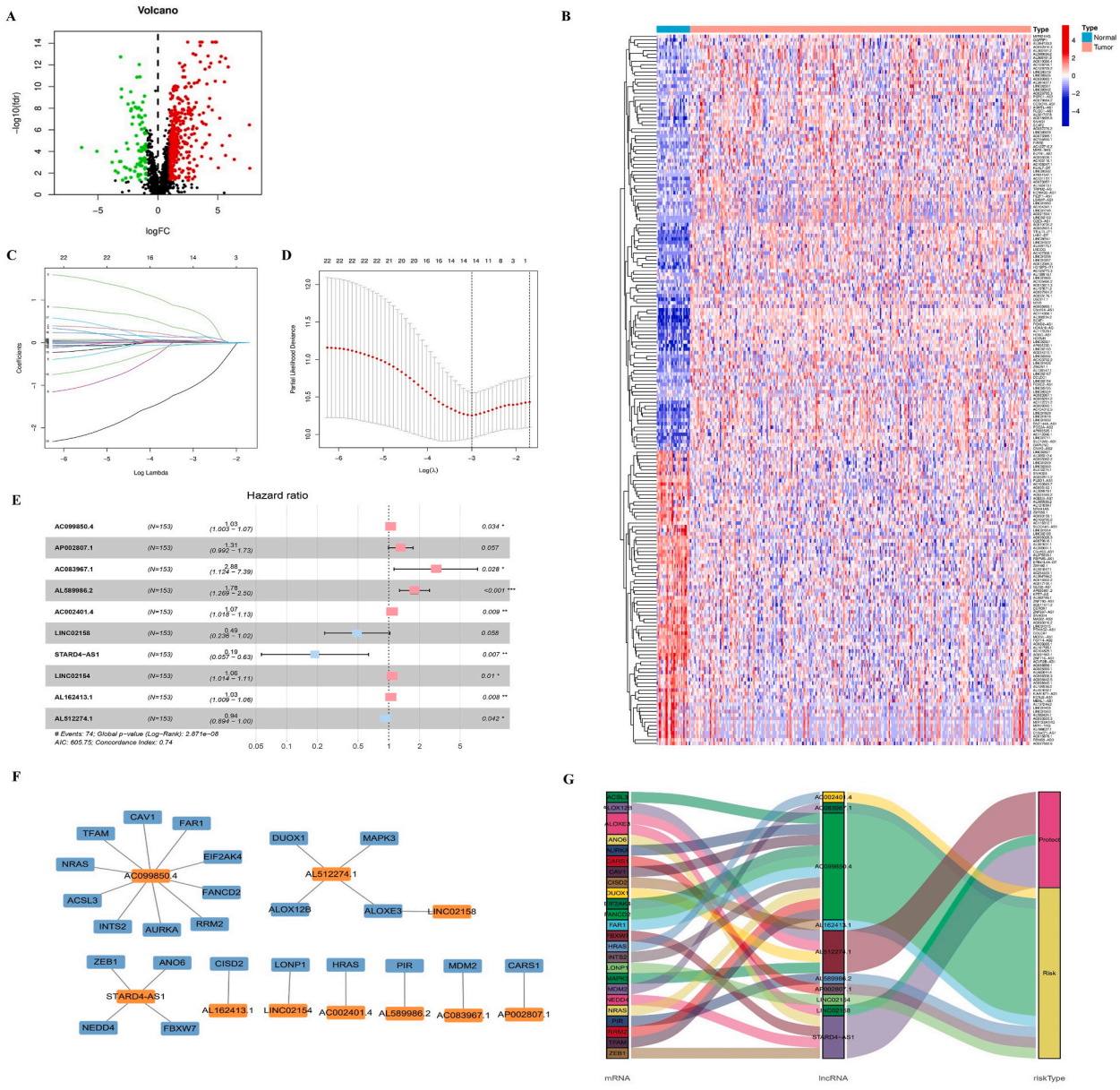

Fig. 3. **A**–**B** Volcano plot and heatmap for the DE-lncRNAs. **C-D** LASSO regression analysis. **E** Forest plots illustrating the relationships of the ten lncRNAs with OS in the training cohort. **F-G** Sankey and co-expression network diagrams of the ferroptosis-related lncRNA–mRNA.

Table 4
Risk scores for 10 lncRNAs included in the prognostic FRL signature.

ID	Coef	HR	HR.95L	HR.95H	Pvalue
AC099850.4	0.034266	1.034860	1.002545	1.068216	0.034261
AP002807.1	0.269102	1.308789	0.991801	1.727089	0.057200
AC083967.1	1.058286	2.881427	1.124188	7.385439	0.027544
AL589986.2	0.577269	1.781168	1.269284	2.499487	0.000840
AC002401.4	0.069336	1.071796	1.017542	1.128943	0.008894
LINC02158	−0.710877	0.491213	0.235838	1.023117	0.057575
STARD4-AS1	−1.666213	0.188961	0.056516	0.631789	0.006818
LINC02154	0.057968	1.059681	1.013922	1.107506	0.010058
AL162413.1	0.034320	1.034915	1.009100	1.061391	0.007749
AL512274.1	−0.057333	0.944280	0.893624	0.997808	0.041553

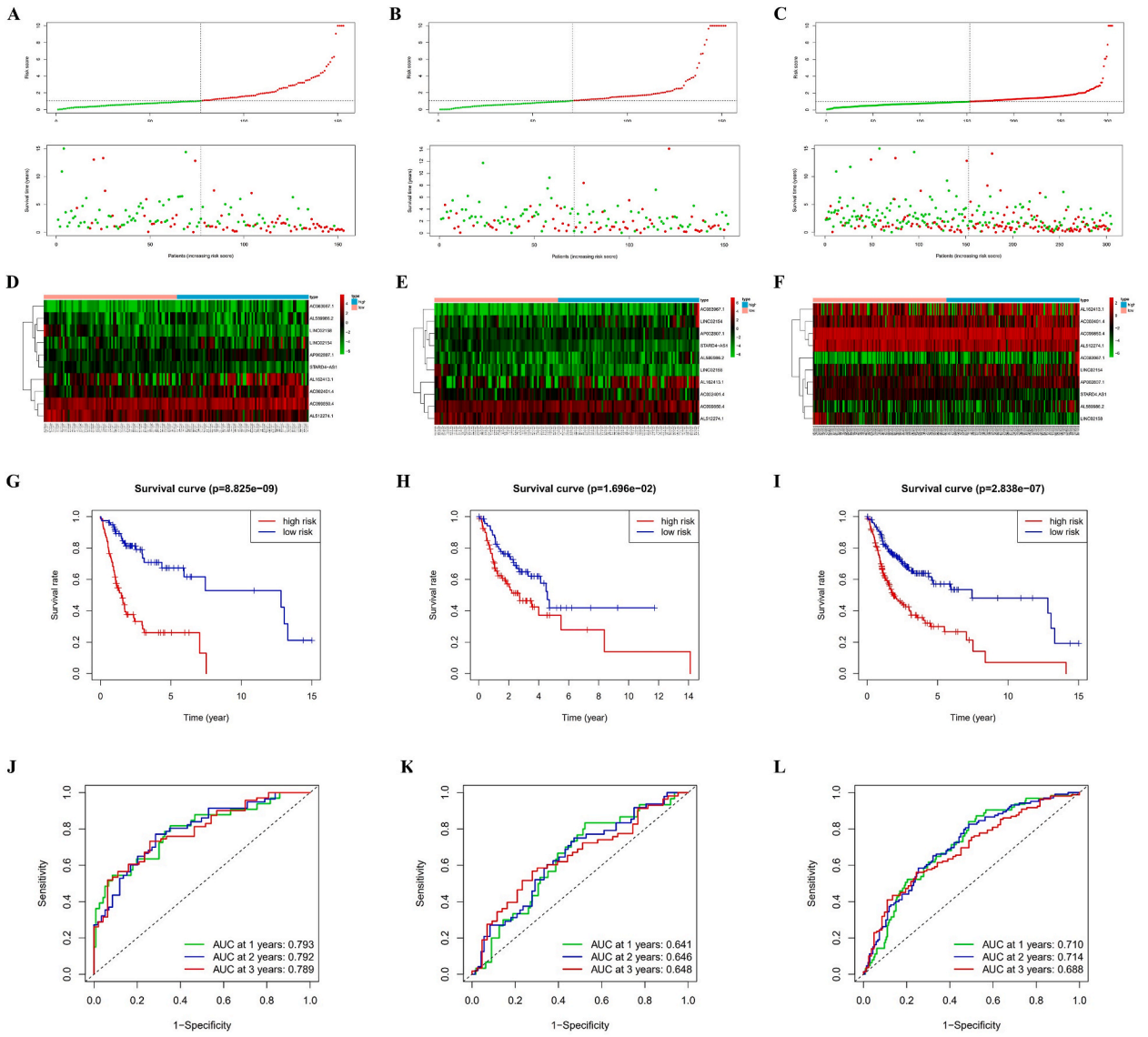

Fig. 4. **A-F** Distribution and heatmap of the risk scores in the training, testing, and entire cohorts. **G-L** Kaplan−Meier curves and ROC curves in the three cohorts.

3.7. Function enrichment analysis

A comprehensive analysis utilizing Gene Ontogeny (GO) pathway enrichment was conducted to elucidate the distinctions among the DE-lncRNAs within the cohorts classified as high and low risk. The outcomes underscored that the signature predominantly regulates processes associated with immunoglobulin receptor binding, immunoglobulin complex, immune response, lymphocytes, and B cell-mediated immunity (Fig. 6A–C). We then performed GSEA on the entire cohort dataset to explore the biological effects of the prognostic FRLs. According to the results, the high-risk cohort was considerably focused on KEGG pathways relating to cancer processes, such as DNA replication, nucleotide excision repair, base excision repair, pyrimidine metabolism, and purine metabolism. In addition, ferroptosis-related pathways, including the metabolism of glutathione, exhibited notable enrichment within the high-risk cohort. Correspondingly, metabolism and immunoreaction-related pathways, focal adhesion, adheres junction, TGF-β signaling pathway, JAK/STAT signaling pathway, T-cell receptor signaling pathway, phosphatidylinositol signaling pathway, and chemokine signaling pathway exhibited apparent enrichment within the low-risk cohort (Fig. 6 D).

3.8. Differential immune cell infiltration and functions in the low- and high-risk cohorts

In exploring the correlation between the risk score and tumor immunity, we conducted ssGSEA analysis, calculating enrichment

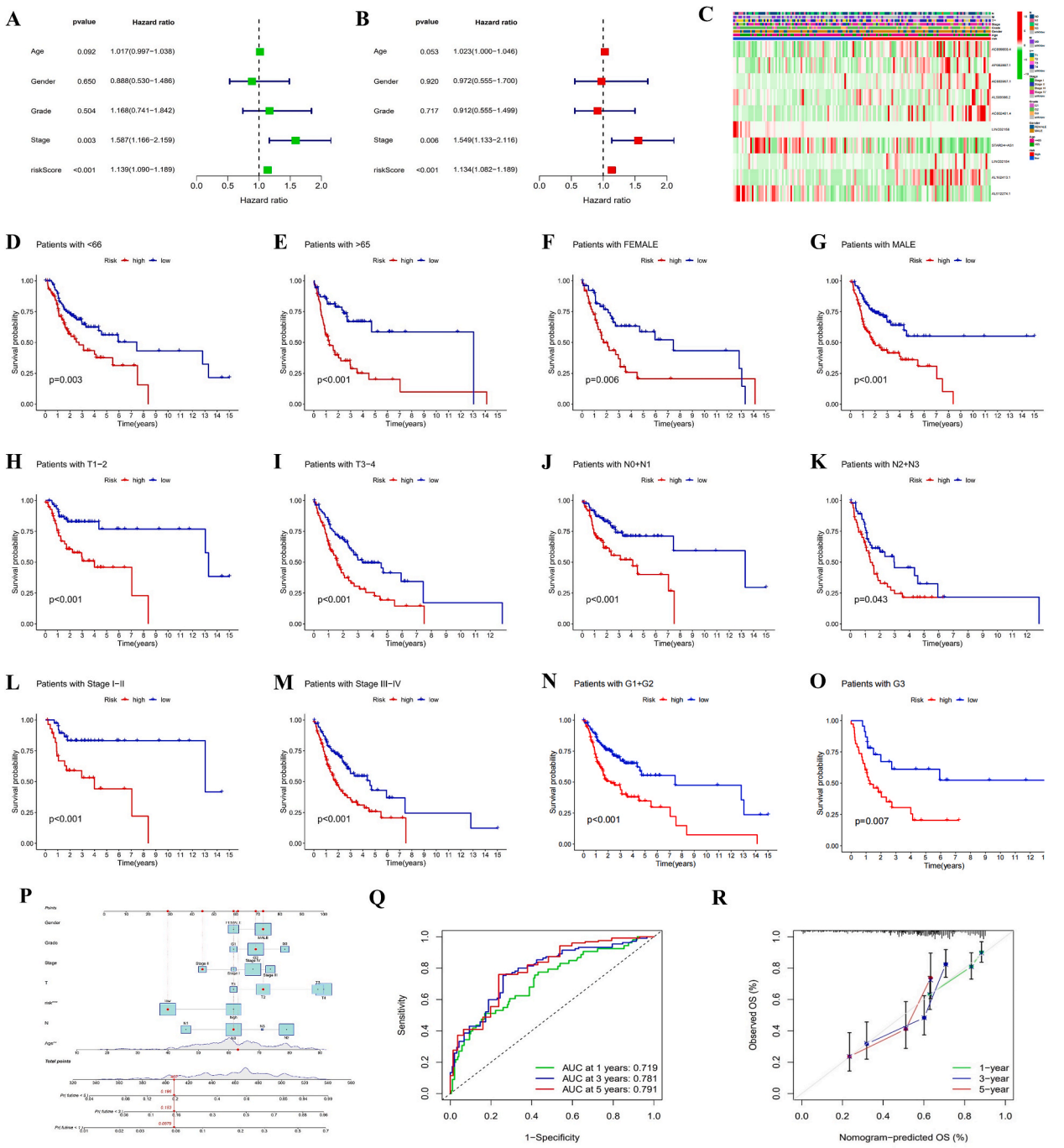

Fig. 5. Identification of FRLs. **A-B** The risk model and clinical features were analyzed using univariate and multivariate Cox regression. **C** Heatmap of FRLs prognostic signature and clinicopathological manifestations. **D-O** Survival differences between the low- and high-risk cohorts classified by clinical characteristics: **D-E** Age (<66 and >65), **F-G** Gender (female and male), **H–I** T Stage (T_{1-2} and T_{3-4}), **J-K** N stage (N_0 and N_{1-3}), **L-M** Tumor stage (I, II III, and IV), **N–O** Tumor grade (G1, G2, and G3). **P** Combined nomogram of FRL prognostic signature and clinicopathologic characteristics. **Q** AUC of time-dependent ROC curves. **R** Calibration curves demonstrate agreement between actual and expected survival rates.

scores across diverse immune cell subpopulations, associated functions, and pathways. The association between risk cohorts and the 22 tumor-infiltrating lymphocytes in OSCC was estimated. The immune response heatmap indicated that T cell $CD4^+$ memory resting, central memory $CD4^+$ T cells, B cells, T cells, cancer-associated fibroblasts, mast cells activated, hematopoietic stem cells, mast cells resting, myeloid dendritic cells, T cells $CD8^+$, monocyte cells, T cells $CD4^+$ Th2, T cells regulatory (Tregs), neutrophils, and endothelial cells were apparent variations between the high- and low-risk cohorts (Fig. 6 E). Immune cell subpopulation correlation analysis

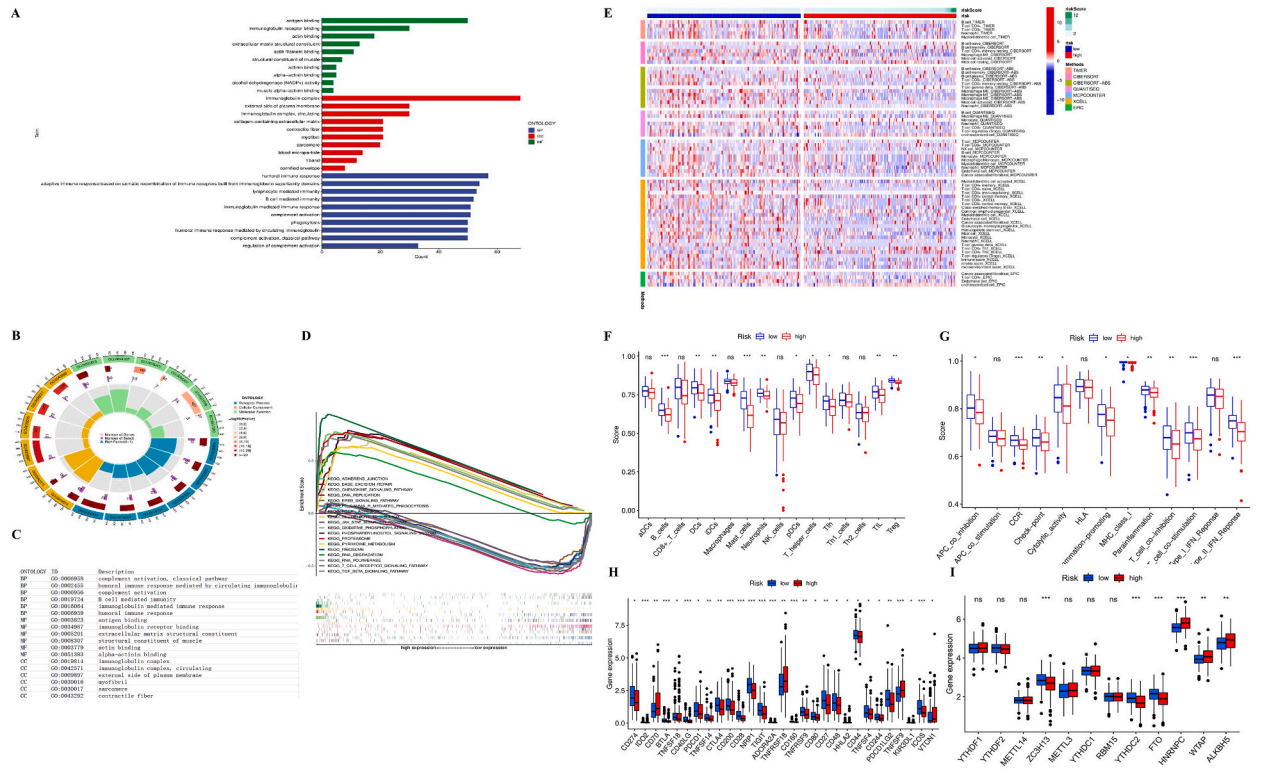

Fig. 6. Comparative functional and immune status analyses between the high- and low-risk cohorts. **A-C** Bar and cluster plot highlighting important GO functional pathways. **D** GSEA. **E** ssGSEA for the correlation between relevant functions and immune cell subsets. **F** The correlations of 13 immune-related functions with the predictive signature. **G** Infiltration levels of 16 immune cells. **H** Boxplots for the immune checkpoint gene comparison. **I** Boxplots for comparing the m6A-related genes.

revealed significant differences in immune cell scores between the two risk cohorts, encompassing B cells, dendritic cells, mast cells, neutrophils, follicular helper T cells, tumor-infiltrating lymphocytes, and Tregs (Fig. 6 F). In addition, immune function scores were significantly variations. CC chemokine receptor, T-cell co-stimulation, type II IFN response, checkpoint, para-inflammation, T-cell co-inhibition, antigen-presenting cell co-inhibition, MHC-class-I, cytolytic-activity, and inflammation-promoting were considerably lower in the high-risk cohort versus the low-risk cohort (Fig. 6 G), suggesting that the risk of OSCC might increase in the absence of these immune.

To research tumor immunotherapy better, the variance in immune checkpoints expression between the two cohorts was investigated using immune checkpoint suppression therapy. The results revealed a marked reduction in the expression levels of most checkpoints within the high-risk cohort in contrast to the low-risk cohort. However, the high-risk cohort exhibited increased expression of five checkpoints (CD70, TNFRSF18, HHLA2, TNFSF9, and VTCN1) (Fig. 6H). This finding suggested that immune checkpoint inhibitors can mitigate the risk of OSCC patients, and the expression of checkpoints in the high-risk cohort was useful in guiding research on these inhibitors and optimizing immunotherapy. Furthermore, we investigated the variances in m6A-related gene expression between the cohorts categorized by risk levels. Our findings demonstrated that, in comparison to the low-risk cohort, the high-risk cohort exhibited higher expression levels of HNRNPC, WTAP, and ALKBH5 (Fig. 6 I).

3.9. Correlation of tumor mutation burden (TMB) with the risk model

The TMB scores were calculated for each risk cohort using the TCGA-OSCC somatic mutation data. The results revealed that, in comparison to the low-risk cohort, the high-risk cohort exhibited higher TMB scores (Fig. 7 A). Fig. 7 B and C indicate the top 20 most highly variable driver genes between the two cohorts. Subsequently, we investigated if TMB functioned as an independent biomarker for OSCC patients. Utilizing the optimal cutoff value for the mutational effect predictor, the entire cohort was split into two cohorts. Patients classified within the low-TMB cohort exhibited longer survival durations compared to those in the high-TMB cohort (Fig. 7 D). However, the integration of the risk score with TMB did not enhance the predictive accuracy for patient survival durations (Fig. 7 E).

3.10. Risk score-based comparison of patient susceptibility to anticancer drugs

The sensitivities of 30 commonly used anticancer medicines were evaluated across high- and low-risk cohorts to discover promising

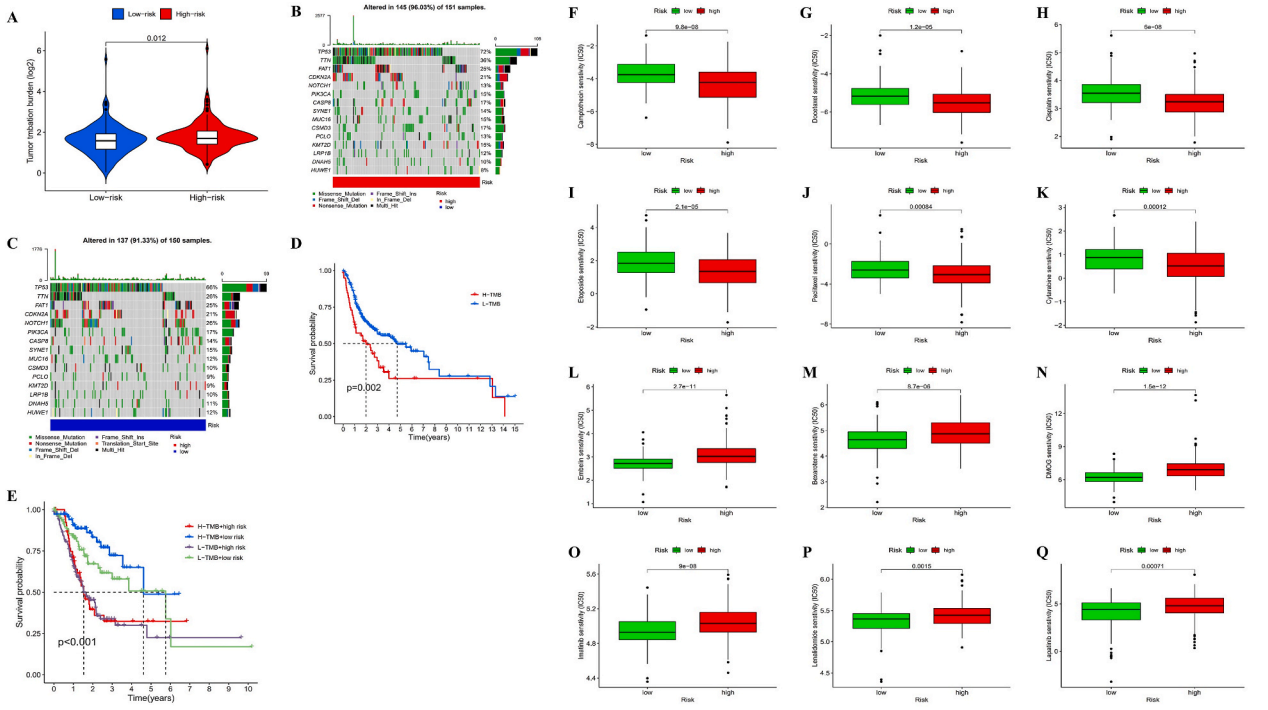

Fig. 7. **A** Discrepancy in TMB between the high- and low-risk cohorts. **B–C** Waterfall plot of the mutation profile for patients with OSCC in two risk cohorts. **D** Survival curves of the two cohorts. **E** Survival curves for patients classified according to TMB and risk signature. **F-Q** The mean differences in the IC50 values of 12 representative medications are displayed in a boxplot (bexarotene, domg, embelin, imatinib, lapatinib, lenalidomide, camptothecin, cisplatin, cytarabine, docetaxel, etoposide, and paclitaxel) between the two risk cohorts.

therapy strategies for OSCC. Fig. 7 F-Q showed 12 representative anticancer drugs. The IC50 values for bexarotene, domg, embelin, imatinib, lapatinib, and lenalidomide were significantly higher in the high-risk cohort compared to the low-risk cohort, showing that these medications appeared to be ineffective for patients classified as high-risk. In contrast, camptothecin, cisplatin, cytarabine, docetaxel, etoposide, and paclitaxel appeared to be the candidate drugs for the treatment of patients classified as high-risk.

3.11. Screening biomarkers

Ten lncRNAs (AC099850.4, AP002807.1, AC083967.1, AL589986.2, AC002401.4, LINC02158, STARD4-AS1, LINC02154, AL162413.1, and AL512274.1) were identified as preliminary biomarkers. AC099850.4, STARD4-AS1, and AL512274.1 were screened out as central lncRNAs (Fig. 3 F). The combined results of KM curves with the log-rank P test indicated that these three lncRNAs were associated with overall survival (Fig. 8A–C). Finally, qRT-PCR results revealed that STARD4-AS1 was highly expressed in SCC9, SCC15, and SCC25 cell lines (Fig. 8 D); therefore, STARD4-AS1 was considered the target lncRNA for subsequent validation.

3.12. Knockdown of STARD4-AS1 inhibited proliferation, migration, and invasion and induced ferroptosis in OSCC cells

In SCC9 and SCC15 cells, siRNA was used to silence STARD4-AS1. STARD4-AS1 transfection efficiency was determined using qRT-PCR to determine its function in OSCC (Fig. 8 E, F). Utilizing the CCK8 assay, we discerned that depletion of STARD4-AS1 elicited a deceleration in cellular proliferation and diminished clonogenic potential across SCC9 and SCC15 cells (Fig. 8 G, H). Comparable outcomes were achieved in the colony formation assay, and a remarkable decline in cell viability was observed in the si-STARD4-AS1 cohort compared to the NC cohort (Fig. 8 I). Subsequently, assays were conducted to assess cell migration and invasion, revealing the impact of si-STARD4-AS1 on OSCC metastasis. As depicted in Fig. 9 A and B, the downregulation of STARD4-AS1 significantly inhibited the migratory and invasive capabilities of SCC9 and SCC15 cells. However, these alterations were found to be reversible by ferroptosis inhibition. In addition, the corresponding values were similar in the STARD4-AS1 si-1 and NC cohorts after adding ferrostatin 1. We then measured the levels of intracellular Fe^{2+} and ROS in OSCC cells after STARD4-AS1 knockdown. Fe^{2+} levels were significantly enhanced in SCC9 and SCC15 cells (Fig. 10 A). The intensity of DCFH-DA indicated that lipid ROS levels were increased in SCC9 and SCC15 cells compared with the vector control (Fig. 10 B). Observations of mitochondrial morphology displayed that, the mitochondrial membranes were ruptured, and cristae disappeared in these cells after STARD4-AS1 knockdown (Fig. 10C). These findings suggested that downregulating STARD4-AS1 inhibited cellular migration and invasion and promoted ferroptosis in OSCC cell lines.

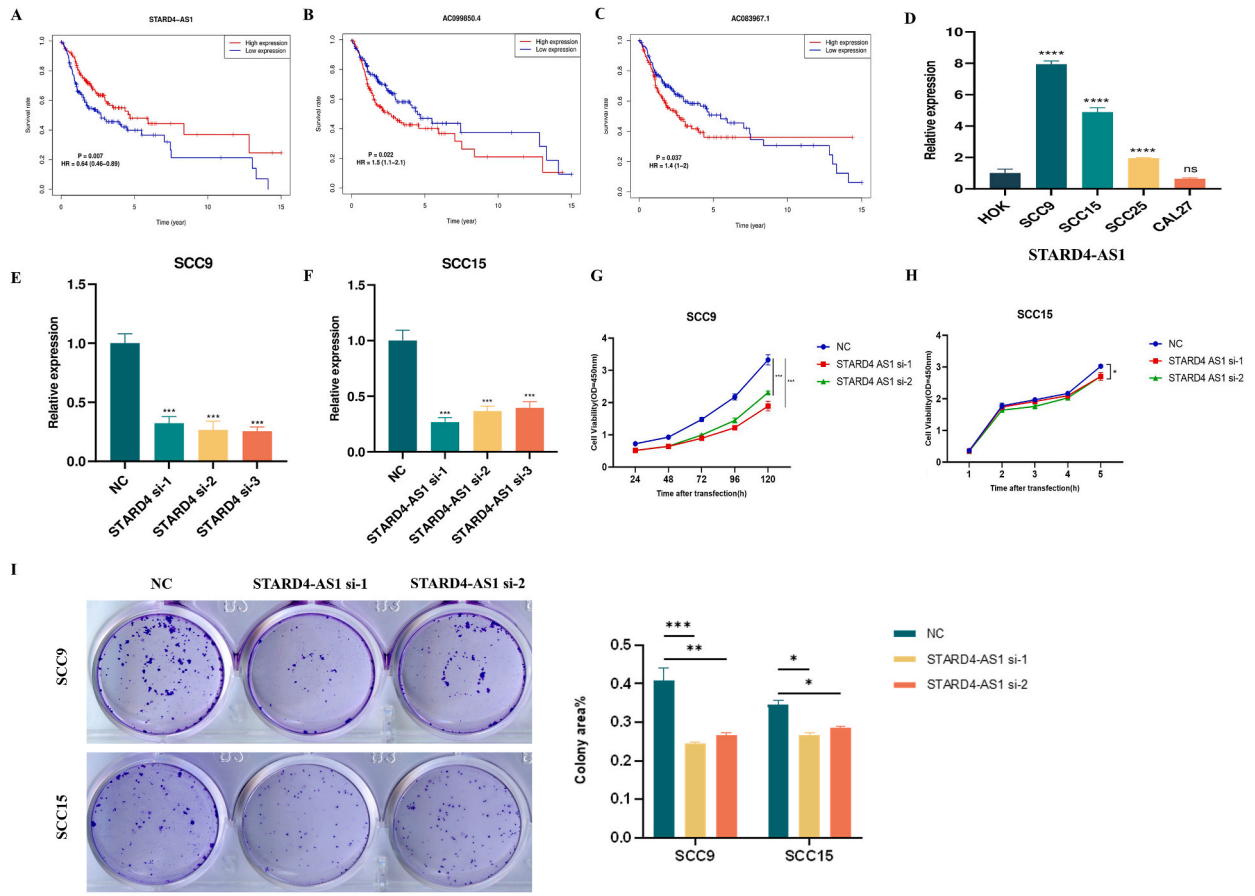

Fig. 8. A-C Overall survival curves of three lncRNAs (AC099850.4, STARD4-AS1, and AC083967.1). **D** Expression patterns of STARD4-AS1 in different cell lines determined using qRT-PCR. **E-I** Downregulation of STARD4-AS1 inhibits OSCC proliferation, migration, and invasion. **E-F** STARD4-AS1 knock down in SCC9 and SCC15 cells. **G-I** STARD4-AS1 knockdown impaired cell proliferation as shown by CCK8 assay (**G-H**) and colony formation assay (**I**).

4. Discussion

Ranked as the sixth most prevalent malignancy worldwide, head and neck squamous cell carcinoma (HNSCC) emerged with nearly one million fresh incidences in 2020 [23]. Primarily occurs on mucosal surfaces, it manifests across four anatomical locales: the oral cavity, nasal cavity, pharynx, and larynx [24]. OSCC is the most common histological subtype of HNSCC with patients having a poor prognosis and high mortality rate, accounting for 90 % of all oral malignancies [25]. The pathogenesis of OSCC has become an active research area to develop new therapeutic targets and strategies for improving the prognosis of OSCC [3,4]. Several molecularly targeted drugs, such as epidermal growth factor receptor and programmed cell death receptor 1 (PD-1) targeted drugs, have been developed for the precision treatment of OSCC [26]. However, available targeted drugs are effective in a limited number of patients and may result in drug resistance and relapse during the treatment. Thus, the identification of reliable and valuable biomarkers for OSCC prognosis is of paramount importance. Iron is the most important nutrient for tumor cell survival, and ferroptosis has a critical role in tumor development [27–30]. In addition, lncRNAs perform a fundamental role in the incidence and progression of distinct tumors. Several lncRNAs have been recognized as promising biomarkers and therapeutic targets for the diagnosis and treatment of malignancies because they are implicated in the occurrence, progression, and medication resistance of malignant tumors [31–33]. Recently, some writers have created FRL-based prediction markers for predicting the prognosis of cancer patients [34–37]. Moreover, ferroptosis is being actively explored as a strategy to combat tumors. However, studies on FRLs in OSCC remain limited, and their impact on patient prognosis needs to be further clarified. In this study, we developed a predictive model comprising 10 FRLs to forecast the prognosis of OSCC patients. Moreover, we identified that lncRNA STARD4-AS1 inhibited ferroptosis and can be used as a novel biomarker for OSCC.

Using univariate Cox, KM, LASSO regression, and multivariate Cox analysis, we constructed a prognostic model based on 10 DE-FRLs. Subsequently, patients were classified into high-risk and low-risk cohorts based on this model. The difference in OS between the cohorts at high and low risk was statistically significant. Through univariate and multivariate Cox analyses, the risk score was determined to be an independent prognostic factor for OSCC. The AUC value of the model was 0.79, indicating that the risk score has

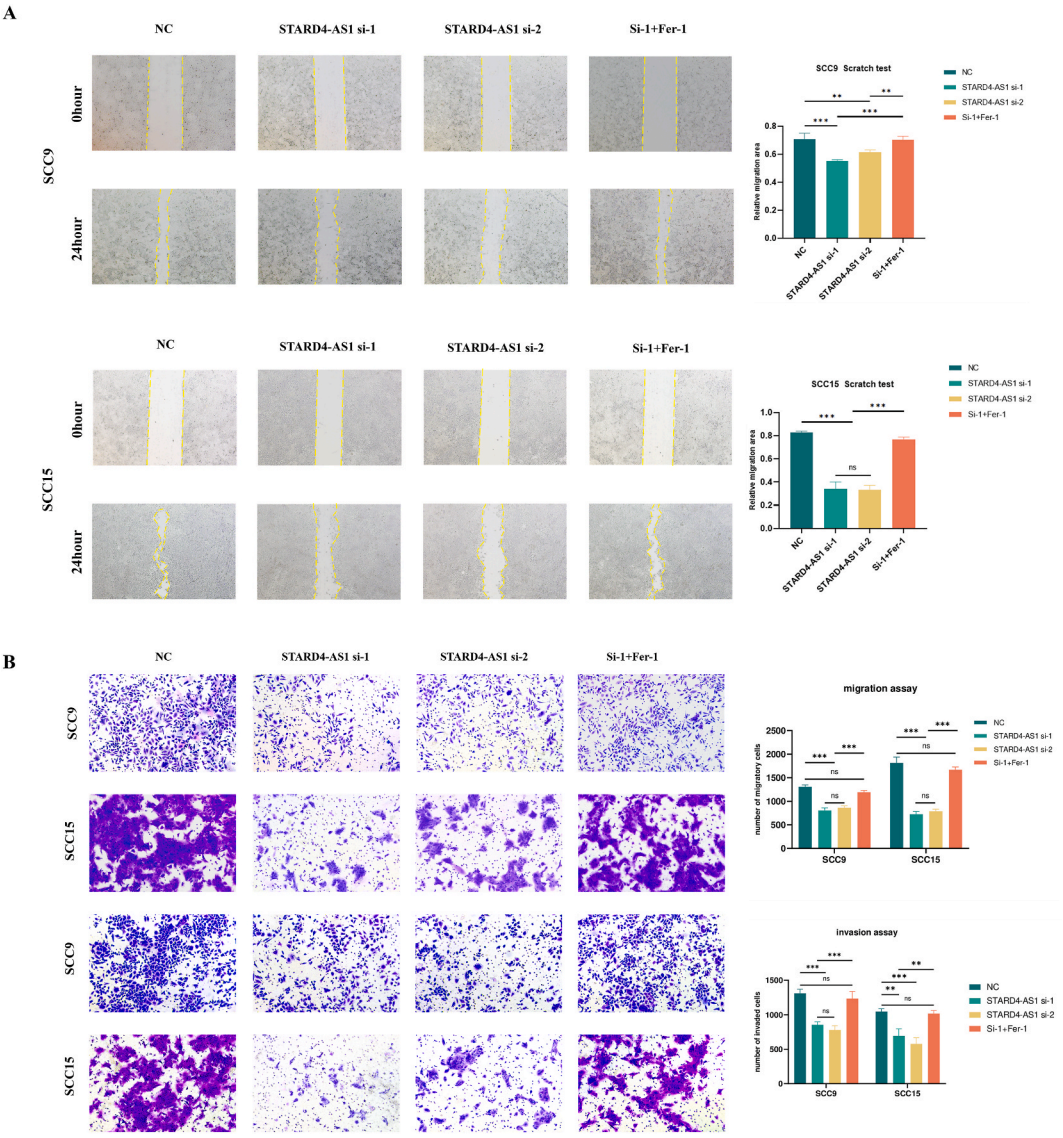

Fig. 9. **A** Results of wound healing assay. **B** Results of migration and invasion assay.

strong predictive ability and that the model is superior to other published models [38,39]. The model showed a greater predictive power for the prognosis of OSCC patients when contrasted with traditional TNM staging. Additionally, to facilitate clinical decision-making, we devised a nomogram integrating this model with clinical features. This model had consistently good predictive ability for both validation and entire datasets. Therefore, our model enhanced the precision of OS prediction for patients with OSCC. These FRLs could be prognostic biomarkers and potential therapeutic targets for OSCC.

Functional enrichment analysis discovered that FRLs correlated with high-risk patients with OSCC were mainly concentrated on processes, encompassing cell cycle, cell nucleotide metabolism, and glutathione metabolism. Aberrant cell cycle progression constitutes a fundamental mechanism in the development of tumors [40–42]. Cancer cell proliferation relies on enhanced cellular nucleotide metabolism, and elevated levels of GSH promote tumor progression and metastasis [43,44]. The findings suggested a tight correlation between FRLs and the occurrence and progression of OSCC. In addition, we used various algorithms to determine immune cell subpopulations considering the correlation between FRLs and immunity. T-cell subsets, multiple B cells, dendritic cells, tumor-infiltrating lymphocytes, cancer-associated fibroblasts, and inflammatory response-associated cells were less infiltrated in the high-risk cohort of patients with OSCC. Recently, Ahmed et al. reported that B cells interact with subpopulations of cancer-associated fibroblasts to facilitate the growth of tumor-associated tertiary lymphoid structures [45]. $CD8^+$ T cells inhibit tumor proliferation by activating ferroptosis in tumor cells [46]. The most effective antigen-presenting cells are dendritic cells, which may stimulate naive T cells and trigger immunological memory reactions in cancer [47]. Taken together, ferroptosis is intricately linked to antitumor immunity in OSCC. Our study revealed significant discrepancies in immune function, immune checkpoints, and m6A-related genes between the two

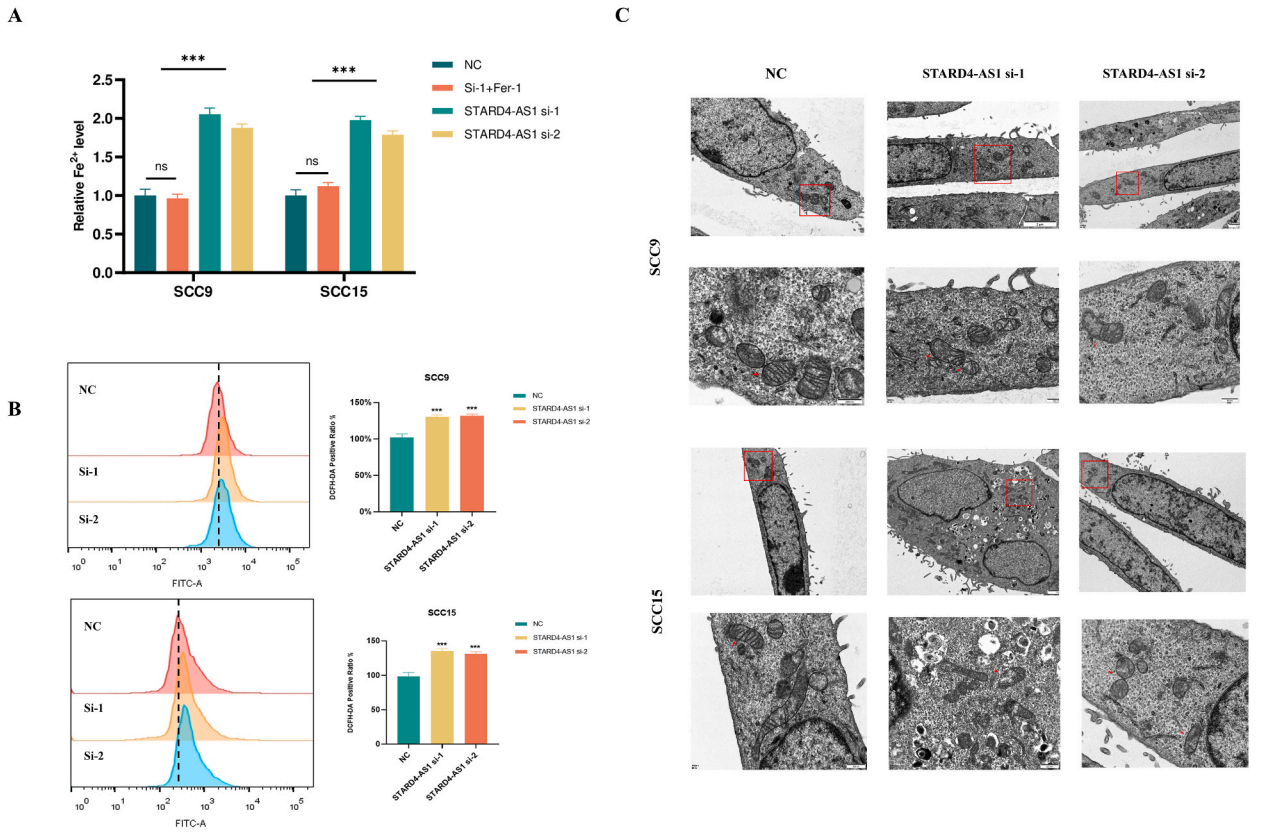

Fig. 10. STARD4-AS1 knockdown significantly inhibits ferroptosis in OSCC cells. **A** Fe^{2+} level. **B** Intracellular ROS level. **C** TEM images show ruptured mitochondrial membrane and disappeared cristae in SCC9 and SCC15 cells after STARD4-AS1 knockdown.

cohorts, offering a theoretical basis for developing personalized immune-targeted therapy for patients with OSCC. TMB has varying prognostic value in different cancer types [48]. Our findings indicated that high TMB was correlated with poor prognosis in OSCC patients. Over recent years, immunotherapy has rapidly advanced, emerging as a widely employed treatment across various malignancies. In addition, immunotherapy combined with chemotherapy is being actively explored. Our model holds promise for guiding the selection of chemotherapy regimens and assessing therapeutic efficacy by comparing the sensitivity of patients to 30 prevalent anticancer drugs across high- and low-risk cohorts. Therefore, our prediction model may reveal reliable immune biomarkers for OSCC treatment in addition to screening chemotherapeutic agents.

Seven of the ten FRLs comprising the prognostic model are the protective factors (AC099850.4, AP002807.1, AC083967.1, AL589986.2, AC002401.4, LINC02154, and AL162413.1), and three of them are risk factors (STARD4-AS1, LINC02158, and AL512274.1). Although most of these FRL signatures have not been reported to date, several of them are associated with cancer development. In head and neck squamous cell carcinoma, the expression of STARD4-AS1 was considerably higher than in surrounding non-tumor tissues, and it had a strong correlation with patient survival. In addition, a diminished expression of STARD4-AS1 exhibited a correlation with poor survival [49]. The Coptis chinensis aqueous extract (CLW) significantly inhibited cell viability, and STARD4-AS1 was downregulated in the human lung adenocarcinoma cell line treated with CLW [50]. However, the relationship of these lncRNAs with ferroptosis needs to be explored. AC099850.4, an immune-related lncRNA, emerged as a promising prognostic biomarker for hepatocellular carcinoma (HCC), exhibiting a positive correlation with the prognosis of HCC patients. In addition, AC099850.4, an m6A modification-related lncRNA, exhibited a positive correlation with the prognosis of cervical cancer patients. Moreover, PD-1 and CTLA-4 were correlated with the expression of AC099850.4 [51,52]. AL512274.1 is negatively related to OSCC prognosis, and its expression is considerably reduced in OSCC. AL512274.1 was localized to the nucleus in an OSCC cell line [53]. AL589986.2 was employed in the construction of a prognostic predictive model for laryngeal cancer, cervical cancer, lung adenocarcinoma, dilated cardiomyopathy, and proliferative vitreoretinopathy [54–58]. LINC02154, significantly expressed in both HCC cells and patient tissues with poor overall survival, has been found to promote HCC proliferation and metastasis by augmenting SPC24 promoter activity and stimulating the PI3K/AKT signaling pathway [59]. In addition, elevated LINC02154 expression was observed in renal and laryngeal squamous cell carcinomas, correlating with a poor prognostic risk factor [60,61]. Nonetheless, its role in oncogenesis remains to be elucidated. These results indicate that a correlation exists between these lncRNAs and the prognosis of patients.

We observed that patients with OSCC had high expression of STARD4-AS1, which correlated with poor prognosis. However, the functions of STARD4-AS1 in OSCC have not been reported to date. Interestingly, the inducible knockdown of STARD4-AS1 markedly

suppressed the migratory and invasive capabilities of SCC9 and SCC15 cells. We determined whether STARD4-AS1 correlates with ferroptosis resistance. Our results revealed that the changes in cell migration and invasion resulting from the knockdown of STARD4-AS1 were reversed by ferroptosis inhibition. In addition, STARD4-AS1 knockdown increased ROS and Fe^{2+} levels. Moreover, mitochondrial membranes were ruptured, and cristae disappeared in OSCC cells after STARD4-AS1 knockdown. Therefore, the knockdown of STARD4-AS1 enhanced erastin-induced ferroptosis in OSCC, suggesting its promise as a novel therapeutic target for OSCC treatment. However, additional investigations are warranted to elucidate the underlying molecular mechanisms.

Our predictive model is a sensitive predictor of the response of patients with OSCC to immunotherapy. In addition, we explored novel biomarkers to aid in the diagnosis and treatment landscape of OSCC. Early identification and risk assessment at the genetic level are indispensable for advancing the precision medicine of patients with OSCC. However, our study has several limitations. First, this model has only been validated in the TCGA dataset, lacking validation across other databases. In forthcoming endeavors, it is imperative to validate the prognostic efficacy of the 10 FRLs signature across additional independent OSCC datasets and larger cohorts of patients. Second, extensive in vivo and in vitro experimental investigations are imperative to authenticate the predictive performance of the 10 FRLs for OSCC prognosis. Finally, even though we have validated that STARD4-AS1 can mediate cellular phenotypes and inhibit ferroptosis, the underlying mechanism by which STARD4-AS1 affects ferroptosis remains unknown. Despite these limitations, the study developed a novel FRL signature and screened a potential ferroptosis suppressor for OSCC, which is correlated with risk and OS in patients with OSCC.

5. Conclusion

We established an FRLs signature, which predicts OSCC prognosis with higher accuracy compared with other available prognostic signatures. In addition, it provides a prognostic nomogram for precision therapy of patients with OSCC. A preliminary correlation between our risk model and the immune microenvironment was identified, and our prediction model assisted in screening chemotherapeutic agents. In vitro analysis suggested that lncRNA STARD4-AS1 may regulate the process of ferroptosis and serve as a novel biomarker of OSCC. Overall, this signature could help provide insights into the possible role of FRLs in OSCC and can be used to design ferroptosis-related targeted therapies. However, the model needs to be verified in future studies.

Funding

This study was supported by the Guangdong Provincial Natural Science Foundation (2024A1515013010) and National Natural Science Foundation of China (82002882).

Data Availability

All data will be made available on request. The datasets for this study can be found in the TCGA (https://portal.gdc.cancer.gov/), and Ensembl (http://asia.ensembl.org), ferroptosis-related-gene can be extracted from the *FerrDb* website (http://www.zhounan.org/ferrdb/). Ferroptosis-related-gene and Ferroptosis-related-lncRNA have been uploaded to the supplemental material.

CRediT authorship contribution statement

Jiahui Li: Writing – review & editing, Writing – original draft, Visualization, Methodology, Formal analysis. **Zihe Qiao:** Writing – review & editing, Visualization, Methodology, Investigation. **Yuwei Li:** Writing – review & editing, Visualization, Validation. **Xinyan Lu:** Writing – review & editing, Visualization, Validation. **Tingru Shao:** Writing – review & editing, Supervision, Funding acquisition, Data curation, Conceptualization. **Xiaozhi Lv:** Writing – review & editing, Writing – original draft, Supervision, Project administration, Funding acquisition, Conceptualization.

Declaration of competing interest

The authors declare that they have no known competing financial interests or personal relationships that could have appeared to influence the work reported in this paper.

Appendix A. Supplementary data

Supplementary data to this article can be found online at https://doi.org/10.1016/j.heliyon.2024.e33193.

References

[1] S.M. Kim, D. Jeong, M.K. Kim, et al., Two different protein expression profiles of oral squamous cell carcinoma were analyzed by immunoprecipitation high-performance liquid chromatography, World J. Surg. Oncol. 15 (1) (2017) 151.
[2] R.L. Siegel, K.D. Miller, H.E. Fuchs, et al., Cancer statistics, CA Cancer J Clin 72 (1) (2022) 7–33, 2022.

[3] C.C. Yu, L.L. Tsai, M.L. Wang, et al., miR145 targets the SOX9/ADAM17 axis to inhibit tumor-initiating cells and IL-6-mediated paracrine effects in head and neck cancer, Cancer Res. 73 (11) (2013) 3425–3440.
[4] M.Y. Chou, F.W. Hu, C.H. Yu, et al., Sox2 expression involvement in the oncogenicity and radiochemoresistance of oral cancer stem cells, Oral Oncol. 51 (1) (2015) 31–39.
[5] B.R. Stockwell, J.P. Friedmann Angeli, H. Bayir, et al., Ferroptosis: a regulated cell death nexus linking metabolism, redox biology, and disease, Cell 171 (2) (2017) 273–285.
[6] J. Tsoi, L. Robert, K. Paraiso, et al., Multi-stage differentiation defines melanoma subtypes with differential vulnerability to drug-induced iron-dependent oxidative stress, Cancer Cell 33 (5) (2018) 890–904 e895.
[7] V.S. Viswanathan, M.J. Ryan, H.D. Dhruv, et al., Dependency of a therapy-resistant state of cancer cells on a lipid peroxidase pathway, Nature 547 (7664) (2017) 453–457.
[8] L.F. Zhou, B. Zhao, L.X. Zhang, et al., Alterations in cellular iron metabolism provide more therapeutic opportunities for cancer, Int. J. Mol. Sci. 19 (5) (2018) 1545.
[9] S.J. Dixon, K.M. Lemberg, M.R. Lamprecht, et al., Ferroptosis: an iron-dependent form of nonapoptotic cell death, Cell 149 (5) (2012) 1060–1072.
[10] J. Li, F. Cao, H.L. Yin, et al., Ferroptosis: past, present and future, Cell Death Dis. 11 (2) (2020) 88.
[11] X. Chen, R. Kang, G. Kroemer, et al., Broadening horizons: the role of ferroptosis in cancer, Nat. Rev. Clin. Oncol. 18 (5) (2021) 280–296.
[12] G. Lei, Y.L. Zhang, P. Koppula, et al., The role of ferroptosis in ionizing radiation-induced cell death and tumor suppression, Cell Res. 30 (2) (2020) 146–162.
[13] Y.H. Mou, J. Wang, J.C. Wu, et al., Ferroptosis, a new form of cell death: opportunities and challenges in cancer, J. Hematol. Oncol. 12 (1) (2019) 34.
[14] J.L. Roh, E.H. Kim, H.J. Jang, et al., Induction of ferroptotic cell death for overcoming cisplatin resistance of head and neck cancer, Cancer Lett. 381 (1) (2016) 96–103.
[15] M.J. Hangauer, V.S. Viswanathan, M.J. Ryan, et al., Drug-tolerant persister cancer cells are vulnerable to GPX4 inhibition, Nature 551 (7679) (2017) 247–250.
[16] C.A. Wicker, B.G. Hunt, S. Krishnan, et al., Glutaminase inhibition with telaglenastat (CB-839) improves treatment response in combination with ionizing radiation in head and neck squamous cell carcinoma models, Cancer Lett. 502 (2021) 180–188.
[17] X.H. Wang, K. Liu, H.M. Gong, et al., Death by histone deacetylase inhibitor quisinostat in tongue squamous cell carcinoma via apoptosis, pyroptosis, and ferroptosis, Toxicol. Appl. Pharmacol. 410 (2021) 115363.
[18] K.J. Huang, Y.H. Wei, Y.C. Chiu, et al., Assessment of zero-valent iron-based nanotherapeutics for ferroptosis induction and resensitization strategy in cancer cells, Biomater. Sci. 7 (4) (2019) 1311–1322.
[19] M.K. Iyer, Y.S. Niknafs, R. Malik, et al., The landscape of long noncoding RNAs in the human transcriptome, Nat. Genet. 47 (3) (2015) 199–208.
[20] J.J. Huang, J. Wang, H. He, et al., Close interactions between lncRNAs, lipid metabolism and ferroptosis in cancer, Int. J. Biol. Sci. 17 (15) (2021) 4493–4513.
[21] C. Mao, X. Wang, Y.T. Liu, et al., A G3BP1-interacting lncRNA promotes ferroptosis and apoptosis in cancer via nuclear sequestration of p53, Cancer Res. 78 (13) (2018) 3484–3496.
[22] Y. Yang, H. Tang, J. Zheng, et al., The PER1/HIF-1alpha negative feedback loop promotes ferroptosis and inhibits tumor progression in oral squamous cell carcinoma, Transl Oncol 18 (2022) 101360.
[23] A. Auperin, Epidemiology of head and neck cancers: an update, Curr. Opin. Oncol. 32 (3) (2020) 178–186.
[24] N. Cohen, S. Fedewa, A.Y. Chen, Epidemiology and demographics of the head and neck cancer population, Oral Maxillofac Surg Clin North Am 30 (4) (2018) 381–395.
[25] A. Zini, R. Czerninski, H.D. Sgan-Cohen, Oral cancer over four decades: epidemiology, trends, histology, and survival by anatomical sites, J. Oral Pathol. Med. 39 (4) (2010) 299–305.
[26] L. Liu, J. Chen, X. Cai, et al., Progress in targeted therapeutic drugs for oral squamous cell carcinoma, Surg Oncol 31 (2019) 90–97.
[27] Q.F. Chen, X.B. Ma, L. Xie, et al., Iron-based nanoparticles for MR imaging-guided ferroptosis in combination with photodynamic therapy to enhance cancer treatment, Nanoscale 13 (9) (2021) 4855–4870.
[28] A. Ghoochani, E.C. Hsu, M. Aslan, et al., Ferroptosis inducers are a novel therapeutic approach for advanced prostate cancer, Cancer Res. 81 (6) (2021) 1583–1594.
[29] Y.F. Hou, S. Cai, S.Y. Yu, et al., Metformin induces ferroptosis by targeting miR-324-3p/GPX4 axis in breast cancer, Acta Biochim. Biophys. Sin. 53 (3) (2021) 333–341.
[30] H.F. Li, L. Li, C. Xue, et al., A novel ferroptosis-related gene signature predicts overall survival of breast cancer patients, Biology 10 (2) (2021) 151.
[31] X. Zhao, X.Y. Li, L.L. Zhou, et al., LncRNA HOXA11-AS drives cisplatin resistance of human LUAD cells via modulating miR-454-3p/Stat3, Cancer Sci. 109 (10) (2018) 3068–3079.
[32] J. Wu, C.L. Zheng, Y.Z. Wang, et al., Correction to: LncRNA APCDD1L-AS1 induces icotinib resistance by inhibition of EGFR autophagic degradation via the miR-1322/miR-1972/miR-324-3p-SIRT5 axis in lung adenocarcinoma, Biomark. Res. 9 (1) (2021) 25.
[33] F.T. Huang, W.Y. Chen, Z.Q. Gu, et al., The novel long intergenic noncoding RNA UCC promotes colorectal cancer progression by sponging miR-143, Cell Death Dis. 8 (5) (2017) e2778.
[34] X.L. Gao, M.B. Tang, S.Y. Tian, et al., A ferroptosis-related gene signature predicts overall survival in patients with lung adenocarcinoma, Future Oncol. 17 (12) (2021) 1533–1544.
[35] K.L. Wang, S.S. Mei, M.C. Cai, et al., Ferroptosis-related long noncoding RNAs as prognostic biomarkers for ovarian cancer, Front. Oncol. 12 (2022) 888699.
[36] Y.R. Wang, S.J. Zhang, Y. Bai, et al., Development and validation of ferroptosis-related LncRNA biomarker in bladder carcinoma, Front. Cell Dev. Biol. 10 (2022) 809747.
[37] Z. Zhang, W.W. Zhang, Y.F. Wang, et al., Construction and validation of a ferroptosis-related lncRNA signature as a novel biomarker for prognosis, immunotherapy and targeted therapy in hepatocellular carcinoma, Front. Cell Dev. Biol. 10 (2022) 792676.
[38] L. Qiu, A. Tao, F. Liu, et al., Potential prognostic value of a eight ferroptosis-related lncRNAs model and the correlative immune activity in oral squamous cell carcinoma, BMC Genom Data 23 (1) (2022) 80.
[39] T. Li, Y. Wang, X. Xiang, et al., Development and validation of a ferroptosis-related lncRNAs prognosis model in oral squamous cell carcinoma, Front. Genet. 13 (2022) 847940.
[40] M. Malumbres, M. Barbacid, Cell cycle, CDKs and cancer: a changing paradigm, Nat. Rev. Cancer 9 (3) (2009) 153–166.
[41] M.B. Kastan, J. Bartek, Cell-cycle checkpoints and cancer, Nature 432 (7015) (2004) 316–323.
[42] J. Liu, Y. Peng, W. Wei, Cell cycle on the crossroad of tumorigenesis and cancer therapy, Trends Cell Biol. 32 (1) (2022) 30–44.
[43] N.J. Mullen, P.K. Singh, Nucleotide metabolism: a pan-cancer metabolic dependency, Nat. Rev. Cancer 23 (5) (2023) 275–294.
[44] A. Bansal, M.C. Simon, Glutathione metabolism in cancer progression and treatment resistance, J. Cell Biol. 217 (7) (2018) 2291–2298.
[45] V. Engelhard, J.R. Conejo-Garcia, R. Ahmed, et al., B cells and cancer, Cancer Cell 39 (10) (2021) 1293–1296.
[46] W. Wang, M. Green, J.E. Choi, et al., CD8(+) T cells regulate tumour ferroptosis during cancer immunotherapy, Nature 569 (7755) (2019) 270–274.
[47] S.K. Wculek, F.J. Cueto, A.M. Mujal, et al., Dendritic cells in cancer immunology and immunotherapy, Nat. Rev. Immunol. 20 (1) (2020) 7–24.
[48] R.M. Samstein, C.H. Lee, A.N. Shoushtari, et al., Tumor mutational load predicts survival after immunotherapy across multiple cancer types, Nat. Genet. 51 (2) (2019) 202–206.
[49] L. Yang, P.G. Lu, X.H. Yang, et al., Excavating novel diagnostic and prognostic long non-coding RNAs (lncRNAs) for head and neck squamous cell carcinoma: an integrated bioinformatics analysis of competing endogenous RNAs (ceRNAs) and gene co-expression networks, Bioengineered 12 (2) (2021) 12821–12838.
[50] A. Maimaiti, J.W. Xu, L.S. Shi, An RNA-seq transcriptome analysis for investigating the anti-lung cancer activity of medicinal Cuscuta chinensis Lam plant, Br. J. Nutr. (2022) 1–13.
[51] J. Wang, Z.R. Jin, G.L. Wu, et al., Bioinformatics analysis for constructing a six-immune-related long noncoding RNA signature as a prognostic model of hepatocellular carcinoma, BioMed Res. Int. 2022 (2022) 2093437.

[52] R. Gu, M. Liu, P. Lin, et al., [Correlation analysis of poor prognosis and immunotherapy of lncRNAs related with m (6)A modification in cervical cancer], Sichuan Da Xue Xue Bao Yi Xue Ban 53 (4) (2022) 626–636.
[53] L. Qiu, A.Q. Tao, F. Liu, et al., Potential prognostic value of a eight ferroptosis-related lncRNAs model and the correlative immune activity in oral squamous cell carcinoma, BMC Genom Data 23 (1) (2022) 80.
[54] G.H. Zhang, E.X. Fan, Q.Y. Zhong, et al., Identification and potential mechanisms of a 4-lncRNA signature that predicts prognosis in patients with laryngeal cancer, Hum Genomics 13 (1) (2019) 36.
[55] J. Ye, X.J. Chen, W.G. Lu, Identification and experimental validation of immune-associate lncRNAs for predicting prognosis in cervical cancer, OncoTargets Ther. 14 (2021) 4721–4734.
[56] Y. Liu, X.S. Zhang, X.C. Cheng, et al., Characterization of fatty acid metabolism-related lncRNAs in lung adenocarcinoma identifying potential novel prognostic targets, Front. Genet. 13 (2022) 990153.
[57] H. Zhang, X.J. Chen, D.F. Zhang, et al., Identification of a novel six-long noncoding RNA signature for molecular diagnosis of dilated cardiomyopathy, DNA Cell Biol. (2020).
[58] Y. Ni, F.Y. Liu, X. Hu, et al., Coding and non-coding RNA interactions reveal immune-related pathways in peripheral blood mononuclear cells derived from patients with proliferative vitreoretinopathy, BMC Med Genomics 14 (1) (2021) 30.
[59] H. Yue, K.F. Wu, K.L. Liu, et al., LINC02154 promotes the proliferation and metastasis of hepatocellular carcinoma by enhancing SPC24 promoter activity and activating the PI3K-AKT signaling pathway, Cell. Oncol. 45 (3) (2022) 447–462.
[60] S.G. Zuo, L.P. Wang, Y. Wen, et al., Identification of a universal 6-lncRNA prognostic signature for three pathologic subtypes of renal cell carcinoma, J. Cell. Biochem. 120 (5) (2019) 7375–7385.
[61] S.Q. Gong, M. Xu, Y.Y. Zhang, et al., The prognostic signature and potential target genes of six long non-coding RNA in laryngeal squamous cell carcinoma, Front. Genet. 11 (2020) 413.